Mixed phase Ti3+-rich TiO2 thin films by oxide defect engineered crystallization

Lauri Palmolahti

lauri.palmolahti@tuni.fi

Tampere University https://orcid.org/0000-0001-9992-6628

Harri Ali-Löytty

Tampere University https://orcid.org/0000-0001-8746-7268

Markku Hannula

Tampere University

Tuomas Tinus

Tampere University https://orcid.org/0000-0002-2397-9544

Kalle Lehtola

Tampere University

Antti Tukiainen

Tampere University

Jarno Reuna

Tampere University

Mika Valden

Tampere University

Article

Keywords:

Posted Date: January 12th, 2024

DOI: https://doi.org/10.21203/rs.3.rs-3772011/v1

Additional Declarations: There is **NO** Competing Interest.

Mixed phase Ti^{3+}-rich TiO_2 thin films by oxide defect engineered crystallization

Lauri Palmolahti[1], Harri Ali-Löytty[1,2*], Markku Hannula[1], Tuomas Tinus[1], Kalle Lehtola[1], Antti Tukiainen[3], Jarno Reuna[3], and Mika Valden[1*]

1) Surface Science Laboratory, Physics Unit, Faculty of Engineering and Natural Sciences, Tampere University, Tampere, Finland

2) Liquid Sun Ltd., Tampere, Finland

3) Faculty of Engineering and Natural Sciences, Tampere University, Tampere, Finland

email: harri.ali-loytty@tuni.fi, mika.valden@tuni.fi

December 15, 2023

Abstract

Amorphous TiO_2 thin films have an insufficient chemical stability for photocatalytic applications. Annealing treatments induce crystallization improving the chemical stability. However, the crystalline structure is already predetermined by the composition of the amorphous phase. In this paper, we demonstrate that the oxide defects, i.e., oxygen vacancies and Ti^{3+} states, can be created by O_2 deficiency during ion-beam sputter deposition without affecting the O/Ti ratio of TiO_2 that thus contains a variable degree of under- and over-coordinated Ti atoms. TiO_2 with only a few defects crystallizes into microcrystalline anatase during vacuum annealing whereas a moderate density of defects causes crystallization into nanocrystalline rutile. An excessive density of defects results in a mixed amorphous/nanocrystalline rutile phase that was analyzed by near-edge x-ray absorption fine structure (NEXAFS) spectroscopy. The density of defects did not affect the crystallization temperature that was 400 °C. Unlike the as deposited amorphous TiO_2 thin films, all crystalline films including the mixed phase one were chemically stable in 1.0 M NaOH. The vacuum annealing preserves the Ti^{3+} gap states that are critical to the charge transfer in protective TiO_2-based photoelectrode coatings.

1 Introduction

The modification of crystal structure and defect composition of TiO_2 thin films has gained a lot of interest as they significantly impact the chemical stability, optical absorption, and charge transfer properties of TiO_2[1, 2, 3, 4, 5]. Anatase and rutile are the two main polymorphs of TiO_2, rutile being thermodynamically the most stable one[6]. The crystallization of TiO_2 is strongly affected by the presence of oxygen vacancies (O_v)[6, 1, 2] and it has been suggested that the O_v in amorphous TiO_2 predetermine to which crystalline phase TiO_2 crystallizes upon annealing[2]. Besides pure phases, mixed-phases have gained interest due to their improved photocatalytic properties[7]. Visible light sensitive black TiO_2 photocatalysts can be fabricated by thermal treatments under non-oxidative conditions[5]. Kang et al. have suggested that an excessive number density of the O_v causes amorphous TiO_2 to crystallize into mixed amorphous–crystalline phase[1].

The formation of an O_v forces three adjacent hexa-coordinated Ti^{4+} atoms to change into pentacoordinated Ti atoms, the two of which change valence state from 4+ to 3+[8, 9, 10]. Thus the O_v defects promote the formation of Ti^{3+} defects. These oxygen defects act as crystallization centers affecting the crystallization of amorphous TiO_2 during annealing[11]. The higher concentration of crystallization centers, the closer the growing crystal grains are to each other. Therefore, increasing the number density of the O_v and Ti^{3+} defects is expected to decrease the resulting crystallite size in annealing induced crystallization. The O_v also decrease the energy required to rearrange the atoms[12]. Because rutile has a lower Gibbs free energy than anatase making it the most stable polymorph[6], and because high O_v concentration has been shown to promote crystallization to rutile through lattice relaxation[13, 6], it is expected that the defect rich amorphous TiO_2 will crystallize into rutile. Annealing in oxygen-free environment, e.g., in ultra-high vacuum, does not oxidize the Ti^{3+} defects thus preserving the exceptional charge transfer properties of Ti^{3+} rich TiO_2.

The O_v can be created by doping, annealing in a reductive environment or with sputtering induced defects[14]. More importantly, the O_v are formed if the deposition of TiO_2 is made under O deficient conditions[2]. Amorphous TiO_2 can be deposited using various methods including atomic layer deposition (ALD), pulsed laser

deposition, and ion-beam sputtering (IBS), in which the number density of the O_v or Ti^{3+} defects can be adjusted by controlling the deposition temperature or the amount of O_2 present during the deposition[4, 2]. The formation of the O_v and Ti^{3+} defects does not necessarily indicate that oxygen atoms are removed from the TiO_2. Interstitial peroxo species can be formed with the formation of the O_v and Ti^{3+} defects thus resulting in defect rich but stoichiometric TiO_2[4, 8].

One potential use for TiO_2 thin films is protective coatings used in artificial photosynthesis to protect the photocatalytic material[15, 16]. The phase structure and defect composition of TiO_2 has been shown to have a significant effect on the chemical stability of TiO_2[4]. Thus, control of the phase composition of TiO_2 via oxide defect engineering can be used tor enhance the chemical stability.

In our earlier research,[4] we have shown that the crystallization of amorphous ALD grown TiO_2 during vacuum annealing depends strongly on the amount of tetrakis(dimethylamino)titanium (TDMAT) precursor fragments and Ti^{3+} defects in TiO_2 film. The decreased amount of precursor fragments and increased number density of Ti^{3+} defects changed the resulting crystal structure from anatase to rutile and decreased the crystallization onset temperature. However, because both amount of precursor fragments and Ti^{3+} defects depend on the deposition temperature it was not possible to differentiate their roles on the crystallization.

In this research the effect of the O_v and Ti^{3+} defects on vacuum annealing induced crystallization of IBS deposited amorphous TiO_2 thin films was investigated. In contrast to ALD, IBS deposition serves as a method to grow TiO_2 thin films with a controlled number density of Ti^{3+} defects but without precursor fragments. The number density of defects ($Ti^{3+}/Ti = 0.1$–10.5 %) in the as deposited samples was controlled by altering the O_2 background flow during the deposition to create O deficient growth environment. The samples were annealed in ultra-high vacuum (200–500 °C) and the chemical composition, crystal structure, and defect concentrations were analyzed after each annealing step with photoelectron spectroscopy and near edge x-ray absorption fine structure (NEXAFS) spectroscopy. The O_2 deficiency during the deposition created Ti^{3+} and O_v defects but surprisingly did not affect the O/Ti ratio of TiO_2. Low concentration of Ti^{3+} defects (0.1 %) resulted in microcrystalline anatase after vacuum annealing, whereas medium concentration (6.4%) resulted in nanocrystalline rutile and high concentration (10.5%) resulted in mixed nanorutile–amorphous phase.

2 Results

2.1 Structural analysis

The effect of the O_2 background flow during the deposition on the structure of the as deposited samples and the samples vacuum annealed at 500 °C was characterized by GIXRD and SEM (Fig. 1). None of the as deposited samples showed any peaks in the GIXRD patterns nor any structure in the SEM images, which indicates amorphous phase. [18]. After annealing in vacuum at 500 °C the TiO_2-40 sample exhibits clear anatase (101) and (200) peaks and the TiO_2-20 sample exhibits wide rutile (110) peak whereas the TiO_2-10 sample did not exhibit any peaks[17]. The FWHM of the rutile (110) peak is 3.0 deg that roughly corresponds to 3 nm crystallite size, whereas the anatase 101 peak has FWHM of 0.7 deg that corresponds to 12 nm crystallite size[19]. The measured GIXRD peak ratios are not the same as for the powder references due to anisotropy. The SEM images show that all of the annealed samples have a clear grain structure. The TiO_2-40 sample exhibits very large (>1 μm) elongated grains whereas TiO_2-20 and TiO_2-10 samples exhibit nano-scale grains (<100 nm) without directional texture. From these results it can be concluded that the TiO_2-40 sample crystallizes into micro-crystalline anatase and the TiO_2-20 sample into nano-crystalline rutile during vacuum annealing. A large area SEM image of the TiO_2-40 sample after annealing is presented in Supplementary Fig. 1 and shows grain lengths up to 10 μm.

The results obtained from the vacuum annealed TiO_2-10 sample are particularly interesting as the SEM images indicated a nano-scale structure, but no GIXRD peaks were observed. This may be due to nano-scale grain size as it can result in such wide and low GIXRD peaks that they become indistinguishable. The structure of the annealed TiO_2-10 sample was further analyzed with NEXAFS spectroscopy as it is more sensitive to the nearest neighbor structure.

The thickness and density of the TiO_2 films were determined from the XRR patterns by fitting the measured pattern with modeled patterns of TiO_2–SiO_2–Si layer structure. The thicknesses of the as deposited TiO_2-40, TiO_2-20, and TiO_2-10 samples were 34.0, 43.2, and 37.8 nm, respectively. After annealing at 500 °C, the thicknesses were slightly smaller: 33.1, 40.6 and 36.5 nm. Based on our test on a thicker sample (60.7 nm), the film thickness had no significant effect on the crystallization or defect formation. The densities are presented in Table 1. The density of TiO_2 increased slightly with increasing oxygen deficiency during the IBS fabrication process as the O_v make the TiO_2 denser by shortening the remaining Ti–O bond lengths[10, 20]. After 500 °C annealing the TiO_2-20 and TiO_2-10 samples had higher densities of 4.00 and 4.01 g/cm^3, respectively, whereas the TiO_2-40 sample had a density of 3.68 g/cm^3. Rutile is denser than anatase[6] so the measured densities imply that the TiO_2-20 and TiO_2-10 samples crystallize into rutile. For the TiO_2-20 sample this is supported by the GIXRD and SEM results.

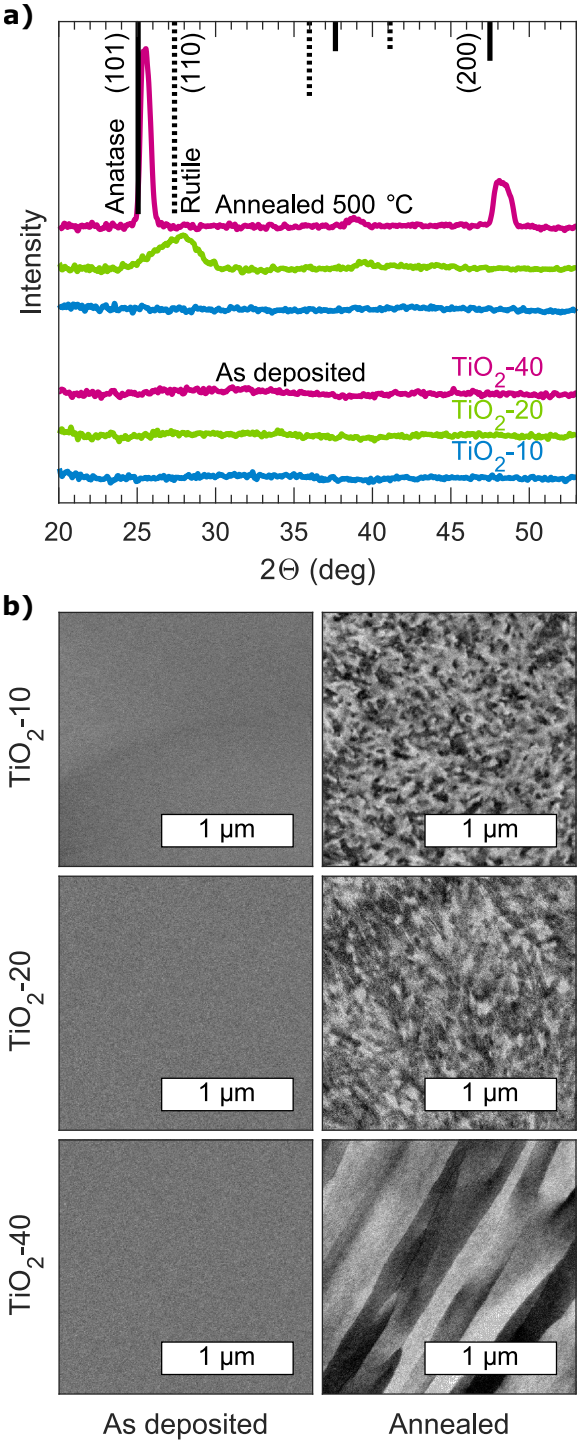

Fig. 1: (a) GIXRD patterns of the as deposited samples and the samples vacuum annealed at 500 °C. Anatase and rutile reference peak positions[17] are shown on top. The height of the reference lines indicates the relative intensity of the reference peaks for powder samples. (b) SEM images of the as deposited samples and the samples vacuum annealed at 500 °C.

Table 1: Properties of all studied samples in the as deposited condition and after vacuum annealing at 500 C. Density is based on XRR modeling (Supplementary Fig. 4) and light absorption coefficient α on UV-vis measurements (Fig. 3). Elemental and chemical state ratios are calculated from the XPS results (Fig. 2).

	TiO_2-40	TiO_2-20	TiO_2-10
	As deposited		
Density (g/cm^3)	3.66	3.78	3.86
α @ 528 nm (10^3/cm)	8.4	22.9	70.9
O/Ti	2.15	2.14	2.15
Ti^{3+}/Ti (%)	0.1	6.4	10.5
O^{1-}/O (%)	3.9	5.0	6.1
Ti^{3+} $3d_{xy}$/VB (%)	0	0	1.4
	Annealed 500 °C		
Density (g/cm^3)	3.68	4.00	4.01
α @ 528 nm (10^3/cm)	47.8	35.6	69.2
O/Ti	2.11	2.15	2.21
Ti^{3+}/Ti (%)	3.7	19.4	41.3
O^{1-}/O (%)	12.6	12.7	19.1
Ti^{3+} $3d_{xy}$/VB (%)	0	1.7	3.9

2.2 Chemical composition and defect concentrations

The chemical composition and defect concentrations of the as deposited samples and samples vacuum annealed at 500 °C were characterized using XPS (Fig. 2). Four elements, O, Ti, C (<7%), and Ar (<0.8%) were detected from the survey spectra (Supplementary Fig. 2). C is an impurity from the atmosphere that is on top of the sample and Ar is from the fabrication process as it is used as a sputtering gas in IBS.

Three chemical states were identified from both O 1s and Ti 2p spectra[4, 21, 8]. The O^{2-} and Ti^{4+} components can be assigned to the TiO_2, whereas the O^{1-} and Ti^{3+} components are related to the O_v and Ti^{3+} defects. The third components are peroxo and Ti^{2+} species, but the amount of these species is small[8]. The in-gap Ti^{3+} $3d_{xy}$ state was identified just below the Fermi level in the valence band spectra.

The Ti^{3+}/Ti, O/Ti, O^{1-}/O, and Ti^{3+} $3d_{xy}$/VB ratios are presented in Table 1 for the as deposited samples and for the samples vacuum annealed at 500 °C. The as deposited TiO_2-40 sample had a negligible number density of Ti^{3+} defects whereas TiO_2-20 had 6.4% and TiO_2-10 sample 10.5%. The number density of Ti^{3+} increased during the annealing. Samples that already had large number density of Ti^{3+} defects had also largest increase in it during the annealing. Unexpectedly the O/Ti ratio was the same for all as deposited samples regardless of the oxygen deficiency during the deposition and the ratio is close to the stoichiometric value of 2 despite the strong difference in the number density of Ti^{3+} defects. Vacuum annealing had a negligible effect on the O/Ti ratio which indicates that O is not removed from the samples during vacuum annealing. Thus, there is no formation of Ti suboxides, e.g., Ti_2O_3, during annealing. This is contraditory to some earlier research where the formation of Ti^{3+} defects is linked to the O deficiency in TiO_2 [22, 23].

O^{1-}/O ratio increases with the number density of Ti^{3+} defects as the charge neutrality principle suggest that equal number density of O^{1-} and Ti^{3+} defects should be formed. This means that O^{1-}/O ratio should be about half of the Ti^{3+}/Ti ratio as there is about twice as many O atoms compared to Ti atoms. However, the annealing increased O^{1-}/O ratio more than the oxygen deficiency during the deposition as can be seen from Table 1.

The formation of Ti^{3+} shifts the Ti^{3+} $3d_{xy}$ energy level from the conduction band to inside the band gap just below the Fermi level due to Jahn–Teller distortion[24]. As the state is now below the Fermi level it becomes occupied which can be seen from the valence band XP-spectra in Fig. 2 and in Table 1. The Ti^{3+} $3d_{xy}$/VB ratio correlates with the Ti^{3+}/Ti ratio. This in-gap state also causes broad band absorption at long wavelengths (>350 nm) as the electrons can be excited from the in-gap state to the conduction band[8]. This broad band absorption can be used to estimate the Ti^{3+} defect concentration in the bulk by measuring the absorption of the TiO_2 thin film deposited on a glass substrate. The absorption coefficient α was calculated from transmission T and reflectance R (Supplementary Fig. 3) using equation $\alpha = -\ln(T/(1-R))/d$, where d is the thickness of the TiO_2 thin film determined from the XRR measurements. The absorption coefficients of the as deposited samples and the samples vacuum annealed at 500 °C are presented as a function of wavelength in Fig. 3. In addition, the band gap values obtained from Tauc-analysis are shown. The wavelength of 528 nm is the focus of interest as the vacuum annealing treatment has been shown to have the strongest effect (decrease) on the defect band absorption at this wavelength. The absorption coefficients at 528 nm corresponding to the absorption of trapped holes in the band gap are shown in Table 1[5]. The absorption clearly shows that in the as deposited samples the defect concentration in bulk follows similar trend with the surface Ti^{3+}/Ti defect concentration and the TiO_2-10 sample has clearly the highest number density of defects both in surface and in bulk whereas

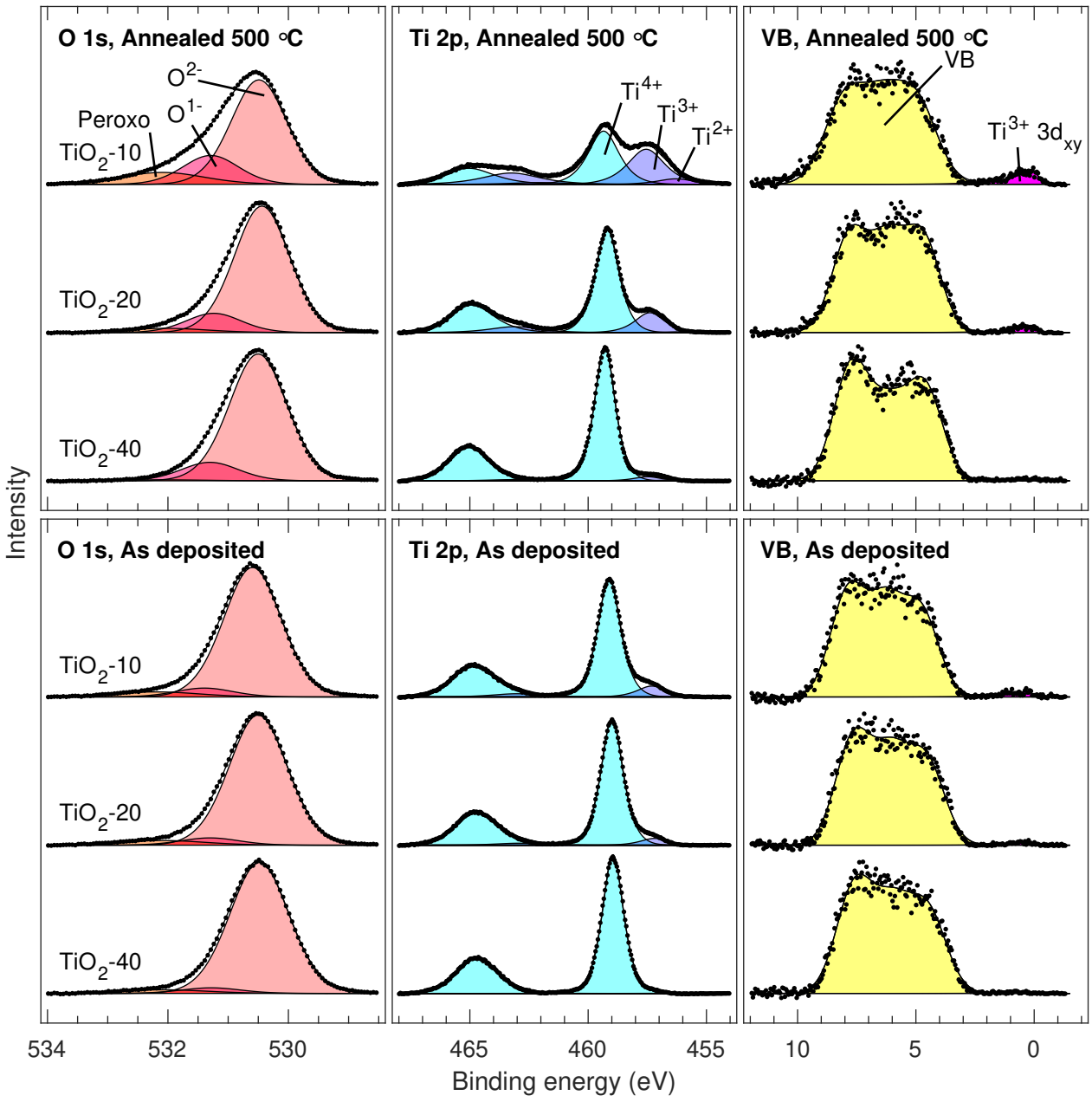

Fig. 2: XP spectra of O 1s, Ti 2p and valence band of the as deposited samples and the samples vacuum annealed at 500 °C. The spectra were measured using Al Kα radiation ($h\nu$ = 1486.6 eV). The intensities are normalized so that each spectrum has the same area.

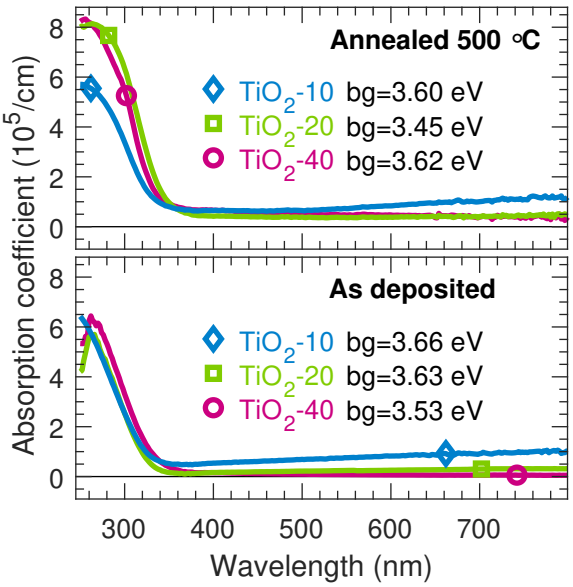

Fig. 3: Absorption coefficient of the as deposited samples and the samples vacuum annealed at 500 °C. Indirect band gap energies were calculated using Tauc-method (Supplementary Fig. 3).

the TiO_2-40 sample has only few defects.

The effect of Ti^{3+}/Ti ratio on the optical absorption is not nearly as consistent for the annealed samples as it is for the as deposited samples. The shape of the in-gap absorption spectra is slightly different for the as deposited and annealed samples as the as deposited samples have a wider in-gap absorption band. Bharti et al. propose that both Ti^{3+} and O_v defects cause a trap state inside the band gap at slightly different energies and that the formation of non-lattice oxygen causes O_v[25]. The annealed samples have higher O^{1-}/O ratio and the optical absorption at 528 nm scales better with the O^{1-}/O ratio than with the Ti^{3+}/Ti ratio. This is consistent with the absorption caused by the trapped holes in the deep gap states while the Ti^{3+} states are shallower closer to the Fermi edge. The results imply that both Ti^{3+} and O_v contribute to the optical absorption.

The band gaps of TiO_2 thin films were analyzed from the UV-vis data using Tauc-method[26, 27]. Indirect band gap was assumed in the Tauc analysis[28]. The band gap values fall within the values reported in the literature[29, 30]. In the as deposited samples the band gap slightly increases with the increasing defect concentration because of the Moss–Burstein effect[31, 8, 5]. As the density of the in-gap defect states just below the conduction band increases, electrons are thermally excited from the detect states to the bottom of the conduction band. As the bottom of the conduction band is now occupied, the optical transition from the valence band to the conduction band needs more energy and the observed absorption edge is shifted to the higher energies. The band gap of rutile is smaller than the band gap of anatase[32]. This further supports the result that the TiO_2-20 sample crystallizes into rutile and the TiO_2-40 sample into anatase as the band gap of the TiO_2-20 sample is smaller than the band gap of the TiO_2-40 sample after vacuum annealing. The TiO_2-10 sample exhibits a large band gap due to the highest concentration of Ti^{3+} defects and the Moss-Burstein effect.

2.3 Structural changes during the post-deposition annealing

NEXAFS spectroscopy was applied to study changes in the local electronic structure during the cumulative annealing series. The phase structure of TiO_2 can be identified from the spectral shape by comparing it to the reference spectra [34]. Both total electron yield (Supplementary Fig. 5 and 6) and Auger electron yield NEXAFS (Supplementary Fig. 7 and 8) were measured to obtain both bulk sensitive and surface sensitive results[35]. The structure of nearest neighbors was determined by comparing the spectral shape of O K-edge and Ti L-edge to the reference spectra of known crystalline structures[5]. The spectra were fitted using the reference spectra of amorphous, anatase, and rutile phases of TiO_2 using the least squares method. The total electron yield spectra after annealing at 200 and 500 °C and the concentration of phases are presented in Fig. 4.

NEXAFS spectroscopy results showed no significant difference between total electron yield and Auger electron yield spectra and thus we conclude that the phase of TiO_2 is more or less the same in the bulk and at the surface. O K-edge total electron yield NEXAFS spectroscopy results show that all of the samples have similar NEXAFS spectra at the beginning of the annealing series. Based on the GIXRD and SEM measurements this phase was identified as amorphous. All samples stayed almost entirely amorphous until the 400 °C annealing temperature. At that temperature the TiO_2-40 sample crystallized into anatase and the TiO_2-20 sample into

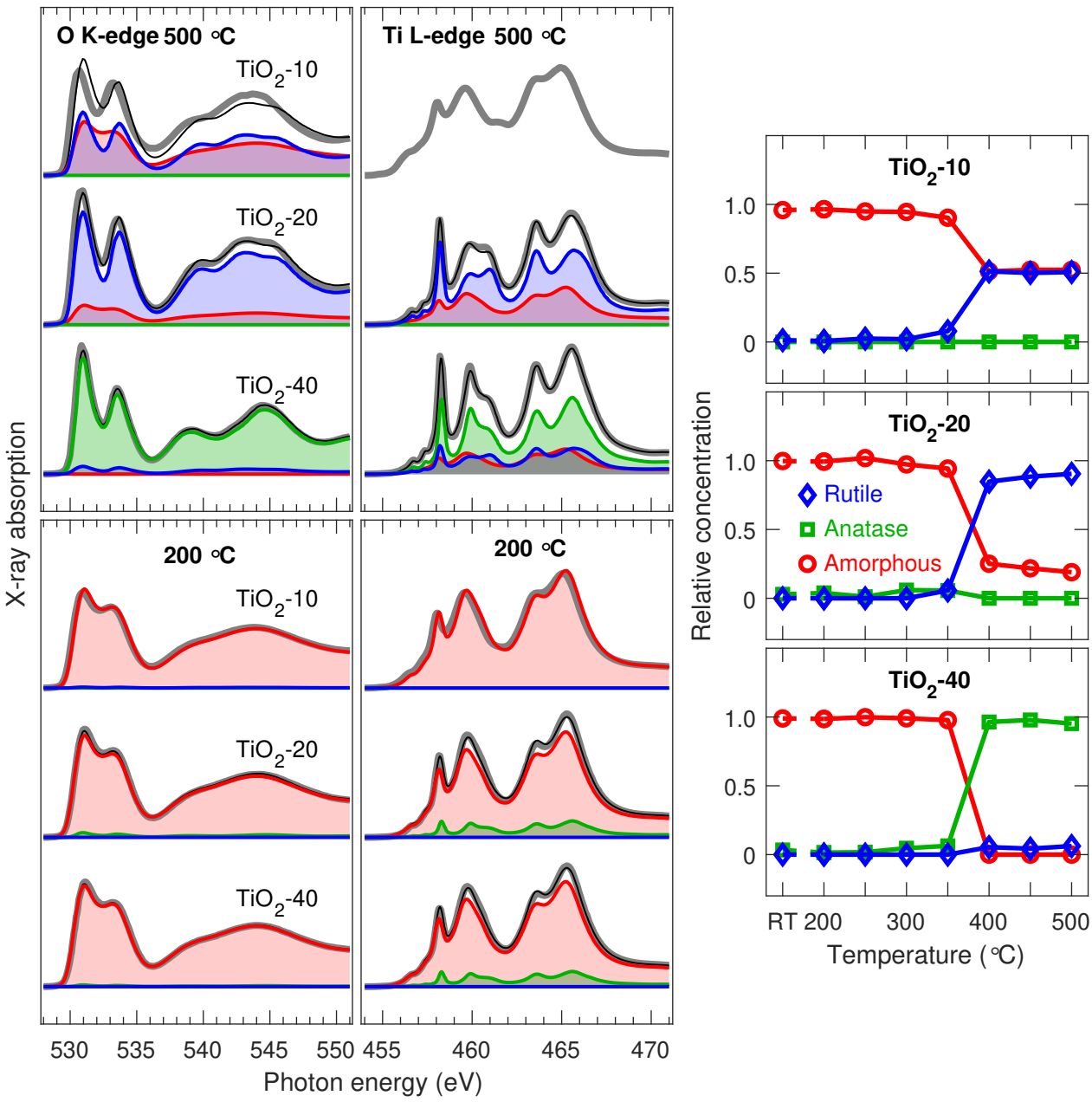

Fig. 4: NEXAFS total electron yield spectra of O K-edge and Ti L-edge measured from the cumulative vacuum annealing series after 200 and 500 °C steps. The thick gray line represents the measured data. The spectra were fitted with amorphous (red), anatase (green) and rutile (blue) reference spectra and the thin black line is the sum of the fitted components. The reference spectra of anatase and rutile were measured from samples with known crystallinity[5, 33], whereas the average of the 200 °C annealed samples was used as a reference for amorphous phase. The concentrations of amorphous, anatase, and rutile phases during the annealing series were calculated from the O K-edge total yield data. All spectra and fittings are presented in Supplementary Fig. 5–8 and the relative concentrations of the phases in Supplementary Fig. 9.

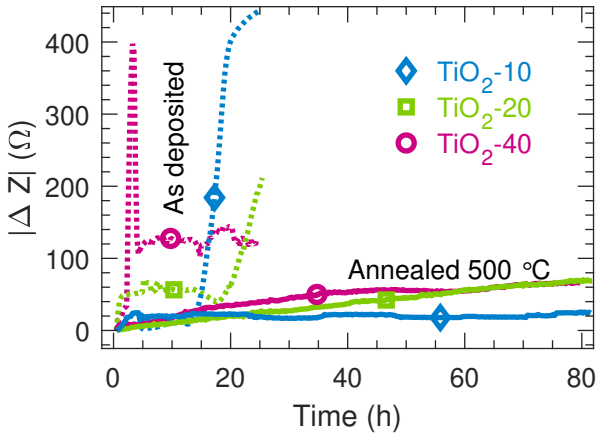

Fig. 5: The change in impedance at 316 Hz during the stability tests in 1.0 M NaOH for the as deposited samples and the samples vacuum annealed at 500 °C.

rutile. This interpretation is also supported by the GIXRD and SEM results. The TiO_2-10 sample had a mixed amorphous and rutile phase after vacuum annealed at 400 °C. The crystallite size of the sample remained below the detection limit of conventional GIXRD but NEXAFS analysis, sensitive to the structure of the nearest neighbors, revealed the partial crystallization.

In all cases the Ti L-edge yielded related results compared to the O K-edge concerning the phase structure. However, the L-edge shape of the TiO_2-10 sample could not be modeled satisfactorily after crystallization using a superposition of the three reference spectra. This method assumes that the regions of different phases are sufficiently large so that the number of atoms near the boundaries of different phases is negligible[36, 35]. In addition, the fitting of the O K-edge of the TiO_2-10 sample after crystallization was not as good as for the other samples and the Ti L-edge had features that were not present in any of the references. Thus, we conclude that the crystallization is only partial resulting in a large number of unit cells that are at the boundary between amorphous and rutile phases. Size dependent effects have been observed in NEXAFS when the crystallite size of TiO_2 is below 10 nm[37, 38]. The results shows that Ti L-edge is more sensitive to the nearest neighbor structure than the O K-edge. In addition, the large number of Ti^{3+} $3d_{xy}$ states may change the density of states about 2–3 eV above the Fermi level[24].

By combining NEXAFS and XPS results, it can be shown that the crystallization of amorphous TiO_2 during vacuum annealing depends on the number density of the O_v and Ti^{3+} defects. TiO_2 with no defects crystallizes into microcrystalline anatase whereas TiO_2 with moderate number density of defects crystallizes into nanocrystalline rutile. Interestingly, the TiO_2 with large number density of defects crystallizes into mixed amorphous/nanocrystalline rutile phase. A similar result has been published for pulse laser deposited TiO_2 films by Yajima et al[2]. They demonstrated that the amorphous TiO_2 deposited in low O_2 pressure (0.1 Pa) results in rutile phase and TiO_2 deposited in moderate O_2 pressure (1 Pa) results in anatase phase after crystallization in 600 °C annealing in N_2. Also, the existence of amorphous domains in defect rich black TiO_2 has been realized by Kang et al[1]. The number density of defects did not affect the crystallization temperature.

2.4 Chemical stability

The protective properties of the TiO_2 thin films were tested by conducting electrochemical impedance spectroscopy (EIS) in 1.0 M NaOH (Supplementary Fig. 10). Figure 5 shows the magnitude of the change of the complex impedance at 316 Hz during the test compared to the value at 0.5 h. The impedance at this frequency reflects the interfacial charge transfer processes within the TiO_2/Si systems[39] and the impedance at 316 Hz was found to be a suitable parameter for monitoring the degradation of the TiO_2/Si electrodes. The results show that the amorphous as deposited TiO_2 thin films are chemically unstable in 1.0 M NaOH as the impedance response changes rapidly already within the first hours. After the stability tests a complete dissolution of the amorphous TiO_2 films was confirmed visually. The vacuum annealed samples were stable for up to 80 h. Interestingly, the annealed TiO_2-10 sample that had the mixed amorphous/noncrystalline rutile structure was chemically stable. Annealing has been shown to also enhance the chemical stability of ALD TiO_2 thin films as well[21].

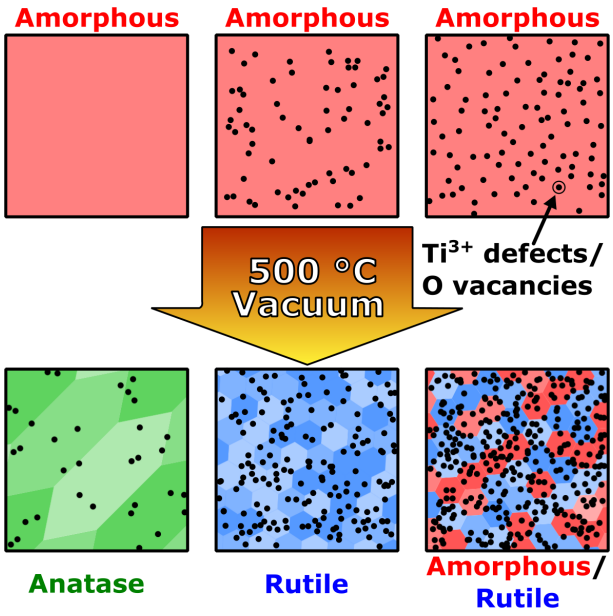

Fig. 6: The effect of the O_v and Ti^{3+} defects on the crystallization of amorphous TiO_2 during vacuum annealing. Unlike the amorphous TiO_2, the crystalline samples, including the amorphous/rutile mixed phase, were chemically stable in 1.0 M NaOH.

3 Discussion

In this research the effect of the O_v and Ti^{3+} defects on vacuum annealing induced crystallization of TiO_2 was studied. Amorphous TiO_2 thin films were deposited using IBS and the O_v and Ti^{3+} defect concentrations were controlled by the O_2 deficiency during the deposition. Interestingly, the O/Ti ratio was found to be close to the stoichiometric value of 2 and was not affected by the O_2 deficiency and the formation of Ti^{3+} defects. The O_v and Ti^{3+} defects induced the formation of in-gap trap states that enhance the charge transfer properties of TiO_2. After annealing in vacuum, the sample with only a few defects crystallized into microcrystalline anatase with elongated grains whereas the sample with moderate number density of defects crystallized into nanocrystalline rutile. More importantly, the sample with excessive number density of defects partially crystallized into rutile thus featuring a mixed amorphous/rutile phase. The effect of the number density of defects on crystallization is summarized in Figure 6. The defect concentration did not affect the crystallization temperature and all of the samples crystallized at 400 °C. No decrease in the O/Ti ratio was observed after vacuum annealing even though the number density of the Ti^{3+} and O_v increased indicating the existence of under- and over-coordinated Ti atoms. Samples with a larger initial number density of Ti^{3+} defects also featured a larger increase in the number density during the vacuum annealing. The vacuum annealing increased the chemical stability of TiO_2 in 1.0 M NaOH drastically. Most importantly, the mixed amorphous/nanocrystalline rutile phase was chemically stable despite the amorphous phase that is typically considered unstable. This demonstrates that the crystallization and chemical stability of TiO_2 can be controlled and engineered using the O_v and Ti^{3+} defects. The high number of in-gap states after annealing due to the O_v and Ti^{3+} defects makes charge transfer properties of TiO_2 thin films suitable for photoelectrode coatings where both high chemical stability and good charge transfer properties are required.

4 Methods

4.1 Sample preparation and characterization

TiO_2 thin films were fabricated using IBS on prepolished p-type Si(100) wafer (Siegert Wafer, B doped). The sputtering was carried out in Navigator 700 (Cutting Edge Coatings GmbH) reactive ion beam sputtering system. Sputtering was performed using an ion beam of an Ar:O_2 mixture with the flow rates of 8 sccm and 0.5 sccm, respectively. The number density of Ti^{3+} defects was controlled by the oxygen deficiency (O_2 background flow) during the deposition. The background O_2 flow that is aimed directly to the sputtering target was varied for each growth using 40, 20, and 10 sccm flow rates and the samples are labeled accordingly as TiO_2-40, TiO_2-20, and TiO_2-10. A 200 mm x 200 mm titanium plate with a purity of 99.8 % was used as the sputtering target. The main sputtering parameters, namely the ion source radiofrequency power, the ion beam current, and the ion beam voltage, were kept constant at 150 W, 230 mA, and 2 kV, respectively. The film thickness was controlled with deposition time that was 353 s for the TiO_2-40 and TiO_2-20 samples. The deposition time

was 217 s for the TiO_2-10 samples to compensate the faster growth rate due to lower O_2 background pressure. Similar sets of TiO_2 thin films were deposited on quartz glass substrates for optical measurements.

The as deposited samples and vacuum annealed samples were characterized using UV–vis spectroscopy (Lambda 1050 UV/VIS/NIR Spectrometer, Perkin Elmer), scanning electron microscopy (SEM, Zeiss Ultra-55), grazing incidence x-ray diffraction (GIXRD) and x-ray reflectivity (XRR, PANalytical X'Pert^3 MRD diffractometer). SEM images were taken using InLens detector and 1 kV acceleration voltage. GIXRD was measured using Cu Kα radiation, 45 kV cathode voltage, and 40 mA cathode current. A 0.02 mm thick Nickel beta filter with attenuation factor of 2.5 was used to attenuate the Cu Kβ peak. XRR was measured in coupled $\omega - 2\theta$ mode. XRR specra were analyzed using GenX program (version 3.5.5)[40]. In the analysis a TiO_2-SiO_2-Si structure was modeled to match the measured reflectance spectra and the densities and thicknesses of the layers and surface roughness was obtained from the fitting parameters. UV–vis transmittance and reflectance spectra were measured using integrating sphere module (150mm InGaAs Int. Sphere).

4.2 X-ray photoelectron spectroscopy

The samples were loaded to NanoESCA photoelectron spectroscopy system (Omicron NanoTechnology GmbH), where x-ray photoelectron spectroscopy (XPS) measurements were performed using monochromatized Al Kα ($h\nu = 1486.6$ eV) excitation source. The samples were cumulatively annealed at 300 and 500 °C in NanoESCA in ultra-high vacuum using radiative heating. The dwell time was 15 minutes, and the temperature was measured with Land Cyclops 160B pyrometer using emissivity of 0.60. XPS spectra were measured before annealing and after both annealing steps. XPS data was fitted with Gaussian/Lorentzian components and Shirley type background subtraction using CasaXPS version 2.3.25PR1.0. O/Ti ratio was calculated from the peak areas using Scofield photoionization cross-sections as relative sensitivity factors[41].

4.3 Near edge x-ray absorption fine structure spectroscopy

A set of as deposited TiO_2 thin films were transferred to the Solid-State End Station (SSES) of the FinEst-BeAMS beamline at MAX IV Laboratory, Lund, Sweden, where NEXAFS was measured[42]. The samples were cumulatively annealed in the preparation chamber of SSES from 200 °C to 500 °C in 50 °C steps. The temperature ramp time and dwell time were both 15 minutes. The annealing was done in ultra-high vacuum ($p<5\times10^{-8}$ mbar) using electron beam bombardment and the temperature was measured with Land Cyclops 160B pyrometer using emissivity of 0.60. The NEXAFS was measured at room temperature in the analysis chamber of SSES before annealing and after each annealing step.

Both bulk sensitive total yield and surface sensitive Auger yield NEXAFS spectra were measured simultaneously. The total yield spectra were measured from the drain current of the sample and the Auger yield from the middle of the corresponding Auger electron peak with 1 s dwell time. The kinetic energy window was 510.8–516.2 eV for O K-edge and 410.8–416.8 eV for Ti L-edge. In both modes photon beam induced current was measured from a gold grid that was positioned in the path of the photon beam. The measured absorption was normalized by this current as the current is proportional to the photon flux. NEXAFS spectra were normalized so that the background level before the absorption edge was set to zero and the edge jump was normalized to one. Reference spectra of anatase, rutile, and amorphous phases were fitted to the data using the least squared method.

4.4 Electrochemical impedance spectroscopy

Electrochemical impedance spectroscopy (EIS) was measured from the as deposited and vacuum annealed TiO_2/Si samples in 1.0 M NaOH (Sigma-Aldrich, Sodium hydroxide, reagent grade). The measurements were done in a custom-made electrochemical cell using three electrode setup with platinum wire as a counter electrode and Leak-Free reference electrode 69-0023 (Harvard Apparatus) as a reference electrode. The sample was used as the working electrode and the area in contact with the electrolyte was sealed using an O-ring with a diameter of 6 mm. The total volume of the cell was 3.5 ml. The measurement was done using Autolab PGSTST12 (Metrohm AG) potentiostat/galvanostat in galvanostatic mode at 0 A. The impedance was measured from 1 MHz to 0.01 Hz using an amplitude of 10 μA. The measurements were repeated every 15 min for 80 h to test the chemical stability of the samples.

References

[1] Jianxin Kang, Yan Zhang, Ziwei Chai, Xiaoyi Qiu, Xingzhong Cao, Peng Zhang, Gilberto Teobaldi, Li-Min Liu, and Lin Guo. Amorphous domains in black titanium dioxide. *Adv. Mater.*, 33(23):2100407, 2021.

[2] Takeaki Yajima, Go Oike, Tomonori Nishimura, and Akira Toriumi. Independent control of phases and defects in TiO_2 thin films for functional transistor channels. *Phys. Status Solidi A*, 213(8):2196–2202, 2016.

[3] Carles Ros, Teresa Andreu, María Dolores Hernández-Alonso, German Penelas-Perez, Jordi Arbiol, and Joan R Morante. Charge transfer characterization of ALD-grown TiO_2 protective layers in silicon photocathodes. *ACS Appl. Mater. Interfaces*, 9(21):17932–17941, 2017.

[4] Lauri Palmolahti, Harri Ali-Löytty, Markku Hannula, Jesse Saari, Weimin Wang, Antti Tukiainen, Kimmo Lahtonen, and Mika Valden. Pinhole-resistant nanocrystalline rutile TiO_2 photoelectrode coatings. *Acta Mater.*, 239:118257, 2022.

[5] Harri Ali-Löytty, Markku Hannula, Jesse Saari, Lauri Palmolahti, Bela D Bhuskute, Riina Ulkuniemi, Tuomo Nyyssönen, Kimmo Lahtonen, and Mika Valden. Diversity of TiO_2: Controlling the molecular and electronic structure of atomic-layer-deposited black TiO_2. *ACS Appl. Mater. Interfaces*, 11(3):2758–2762, 2019.

[6] Dorian AH Hanaor and Charles C Sorrell. Review of the anatase to rutile phase transformation. *J. Mater. Sci.*, 46(4):855–874, 2011.

[7] David O Scanlon, Charles W Dunnill, John Buckeridge, Stephen A Shevlin, Andrew J Logsdail, Scott M Woodley, C Richard A Catlow, Michael J Powell, Robert G Palgrave, Ivan P Parkin, et al. Band alignment of rutile and anatase TiO_2. *Nat. Mater.*, 12(9):798–801, 2013.

[8] Jesse Saari, Harri Ali-Löytty, Minttu Maria Kauppinen, Markku Hannula, Ramsha Khan, Kimmo Lahtonen, Lauri Palmolahti, Antti Tukiainen, Henrik Gronbeck, Nikolai V Tkachenko, et al. Tunable Ti^{3+}-mediated charge carrier dynamics of atomic layer deposition-grown amorphous TiO_2. *J. Phys. Chem. C*, 126(9):4542–4554, 2022.

[9] Fabio G Santomauro, Andrea Lübcke, Jochen Rittmann, E Baldini, A Ferrer, M Silatani, P Zimmermann, Sebastian Grübel, Jeremy A Johnson, Simon O Mariager, et al. Femtosecond X-ray absorption study of electron localization in photoexcited anatase TiO_2. *Sci. Rep.*, 5(1):14834, 2015.

[10] Benjamin J Morgan and Graeme W Watson. A density functional theory + U study of oxygen vacancy formation at the (110), (100), (101), and (001) surfaces of rutile TiO_2. *J. Phys. Chem. C*, 113(17):7322–7328, 2009.

[11] Biswajit Choudhury and Amarjyoti Choudhury. Local structure modification and phase transformation of tio 2 nanoparticles initiated by oxygen defects, grain size, and annealing temperature. *Int. Nano Lett.*, 3:1–9, 2013.

[12] Robert D Shannon and Joseph A Pask. Kinetics of the anatase-rutile transformation. *J. Am. Ceram. Soc.*, 48(8):391–398, 1965.

[13] Chandana Rath, P Mohanty, AC Pandey, and NC Mishra. Oxygen vacancy induced structural phase transformation in TiO_2 nanoparticles. *J. Phys. D: Appl. Phys.*, 42(20):205101, 2009.

[14] Ken Onda, Bin Li, and Hrvoje Petek. Two-photon photoemission spectroscopy of TiO_2(110) surfaces modified by defects and O_2 or H_2O adsorbates. *Phys. Rev. B*, 70(4):045415, 2004.

[15] Thomas Moehl, Jihye Suh, Laurent Severy, Rene Wick-Joliat, and S David Tilley. Investigation of (leaky) ALD TiO_2 protection layers for water-splitting photoelectrodes. *ACS Appl. Mater. Interfaces*, 9(50):43614–43622, 2017.

[16] Huimin Li, Tuo Wang, Shanshan Liu, Zhibin Luo, Lulu Li, Huaiyuan Wang, Zhi-Jian Zhao, and Jinlong Gong. Controllable distribution of oxygen vacancies in grain boundaries of p-Si/TiO_2 heterojunction photocathodes for solar water splitting. *Angew. Chem. Int. Ed.*, 60(8):4034–4037, 2021.

[17] Barbara Lafuente, R. T. Downs, H. Yang, and N. Stone. *1. The power of databases: The RRUFF project*, pages 1–30. De Gruyter (O), Berlin, München, Boston, 2016.

[18] S Sankar and KG Gopchandran. Effect of annealing on the structural, electrical and optical properties of nanostructured TiO_2 thin films. *Cryst. Res. Technol.*, 44(9):989–994, 2009.

[19] XRD crystallite (grain) size calculator (Scherrer equation) – InstaNANO. https://instanano.com/all/-characterization/xrd/crystallite-size, Accessed 26.7.2023.

[20] Sheng-Guang Wang, Xiao-Dong Wen, Dong-Bo Cao, Yong-Wang Li, Jianguo Wang, and Haijun Jiao. Formation of oxygen vacancies on the TiO_2 (110) surfaces. *Surf. Sci.*, 577(1):69–76, 2005.

[21] Markku Hannula, Harri Ali-Löytty, Kimmo Lahtonen, Essi Sarlin, Jesse Saari, and Mika Valden. Improved stability of atomic layer deposited amorphous TiO_2 photoelectrode coatings by thermally induced oxygen defects. *Chem. Mater.*, 30(4):1199–1208, 2018.

[22] SA Abdullah, MZ Sahdan, N Nafarizal, H Saim, Z Embong, CH Cik Rohaida, and F Adriyanto. Influence of substrate annealing on inducing Ti^{3+} and oxygen vacancy in TiO_2 thin films deposited via RF magnetron sputtering. *Appl. Surf. Sci.*, 462:575–582, 2018.

[23] Guangquan Lu, Amy Linsebigler, and John T Yates Jr. Ti^{3+} defect sites on TiO_2(110): production and chemical detection of active sites. *J. Phys. Chem.*, 98(45):11733–11738, 1994.

[24] Zhiqiang Wang, Bo Wen, Qunqing Hao, Li-Min Liu, Chuanyao Zhou, Xinchun Mao, Xiufeng Lang, Wen-Jin Yin, Dongxu Dai, Annabella Selloni, et al. Localized excitation of Ti^{3+} ions in the photoabsorption and photocatalytic activity of reduced rutile TiO_2. *J. Am. Chem. Soc.*, 137(28):9146–9152, 2015.

[25] Bandna Bharti, Santosh Kumar, Heung-No Lee, and Rajesh Kumar. Formation of oxygen vacancies and Ti^{3+} state in TiO_2 thin film and enhanced optical properties by air plasma treatment. *Sci. Rep.*, 6(1):32355, 2016.

[26] Patrycja Makuła, Michał Pacia, and Wojciech Macyk. How to correctly determine the band gap energy of modified semiconductor photocatalysts based on UV–Vis spectra. *J. Phys. Chem. Lett.*, 9(23):6814–6817, 2018.

[27] J Tauc, Radu Grigorovici, and Anina Vancu. Optical properties and electronic structure of amorphous germanium. *Phys. Status Solidi B*, 15(2):627–637, 1966.

[28] Chinedu E Ekuma and Diola Bagayoko. Ab-initio electronic and structural properties of rutile titanium dioxide. *Jpn. J. Appl. Phys.*, 50(10R):101103, 2011.

[29] P Chrysicopoulou, D Davazoglou, Chr Trapalis, and G Kordas. Optical properties of very thin (< 100 nm) sol–gel TiO_2 films. *Thin solid films*, 323(1-2):188–193, 1998.

[30] M Landmann, EWGS Rauls, and WG Schmidt. The electronic structure and optical response of rutile, anatase and brookite TiO_2. *J. Phys.: Condens. Matter*, 24(19):195503, 2012.

[31] Elias Burstein. Anomalous optical absorption limit in InSb. *Phys. Rev.*, 93(3):632, 1954.

[32] Yoshio Nosaka and Atsuko Y Nosaka. Reconsideration of intrinsic band alignments within anatase and rutile TiO_2. *J. Phys. Chem. Lett.*, 7(3):431–434, 2016.

[33] Ramsha Khan, Harri Ali-Löytty, Jesse Saari, Mika Valden, Antti Tukiainen, Kimmo Lahtonen, and Nikolai V Tkachenko. Optimization of photogenerated charge carrier lifetimes in ALD grown TiO_2 for photonic applications. *Nanomater.*, 10(8):1567, 2020.

[34] Matthew Newville. Fundamentals of XAFS. *Rev. Mineral. Geochem.*, 78(1):33–74, 2014.

[35] J.G. Chen. NEXAFS investigations of transition metal oxides, nitrides, carbides, sulfides and other interstitial compounds. *Surface Science Reports*, 30(1):1–152, 1997.

[36] Tod A Pascal, Kevin H Wujcik, Juan Velasco-Velez, Chenghao Wu, Alexander A Teran, Mukes Kapilashrami, Jordi Cabana, Jinghua Guo, Miquel Salmeron, Nitash Balsara, et al. X-ray absorption spectra of dissolved polysulfides in lithium–sulfur batteries from first-principles. *J. Phys. Chem. Lett.*, 5(9):1547–1551, 2014.

[37] Alexei Kuzmin and Jesús Chaboy. EXAFS and XANES analysis of oxides at the nanoscale. *IUCrJ*, 1(6):571–589, 2014.

[38] Hyun Chul Choi, Hyo-Jin Ahn, Young Mee Jung, Min Kyu Lee, Hyun Joon Shin, Seung Bin Kim, and Yung-Eun Sung. Characterization of the structures of size-selected TiO_2 nanoparticles using x-ray absorption spectroscopy. *Appl. Spectrosc.*, 58(5):598–602, 2004.

[39] M Hannula, H Ali-Löytty, K Lahtonen, J Saari, A Tukiainen, and M Valden. Highly efficient charge separation in model Z-scheme $TiO_2/TiSi_2/Si$ photoanode by micropatterned titanium silicide interlayer. *Acta Mater.*, 174:237–245, 2019.

[40] Matts Björck and Gabriella Andersson. GenX: An extensible X-ray reflectivity refinement program utilizing differential evolution. *J. Appl. Crystallogr.*, 40(6):1174–1178, 2007.

[41] James H Scofield. Hartree-Slater subshell photoionization cross-sections at 1254 and 1487 eV. *J. Electron. Spectrosc. Relat. Phenom.*, 8(2):129–137, 1976.

[42] R Pärna, R Sankari, E Kukk, E Nõmmiste, M Valden, M Lastusaari, K Kooser, K Kokko, M Hirsimäki, S Urpelainen, et al. FinEstBeaMS – a wide-range Finnish-Estonian beamline for materials science at the 1.5 GeV storage ring at the MAX IV Laboratory. *Nucl. Instrum. Methods Phys. Res. Sect. A*, 859:83–89, 2017.

5 Acknowledgments

The authors thank Marika Janka for part of the IBS depositions. This work was supported by the Academy of Finland (Decision No. 326461), the Jane & Aatos Erkko Foundation (project "SOFUS"), and Business Finland (Decision No. 1464/31/2019). L.P. was supported by the KAUTE Foundation, Finnish Cultural Foundation, and Vilho, Yrjö and Kalle Väisälä Foundation of the Finnish Academy of Science and Letters. H.A.-L. was supported by the Jenny and Antti Wihuri Foundation. T.T. was supported by the Academy of Finland (Decision No. 339545, nSTAR consortium). This work is part of the Academy of Finland Flagship Programme, Photonics Research and Innovation (PREIN) (Decision No. 320165). We acknowledge MAX IV Laboratory for time on Beamline FinEstBeAMS under Proposals 20220486 and 20221303. Research conducted at MAX IV, a Swedish national user facility, is supported by the Swedish Research council under contract 2018-07152, the Swedish Governmental Agency for Innovation Systems under contract 2018-04969, and Formas under contract 2019-02496.

6 Author contributions

J.R. fabricated the samples. L.P., M.H., and T.T. measured XAS and A.T. measured GIXRD and XRR. M.H. measured XPS and K.L. performed the stability tests. L.P. measured SEM and UV-vis, wrote the original draft of the manuscript and analyzed and visualized the data. H.A.-L. analyzed the XRR data. H.A.-L., M.H., K.L., and M.V. participated to editing of the manuscript. M.V. and H.A.-L. supervised the work.

7 Competing interests

The authors declare no competing interests.

8 Additional information

Supplementary information The online version contains supplementary material available at .

Correspondence and requests for materials should be addressed to Mika Valden and Harri Ali-Löytty.

Supplementary Files

This is a list of supplementary files associated with this preprint. Click to download.

- palmolahti2023suppinfo.pdf